Supplementary Information for

Absence of Ce^{3+} Sites in Chemically Active Colloidal Ceria Nanoparticles

Jean-Daniel Cafun,[1] Kristina O. Kvashnina,[1] Eudald Casals,[2,3] Víctor F. Puntes [2,3*] & Pieter Glatzel[1*]

[1]European Synchrotron Radiation facility (ESRF), BP 220, 6 Rue Jules Horowitz, 38043 Grenoble, France.

[2] Instutut Català de Nanotecnologia (ICN), Campus de la UAB, 08193 Bellatera, Spain.

[3] Universitat Autònoma de Barcelona (UAB),Campus UAB, 08193 Bellaterra, Spain.

*Correspondence to: pieter.glatzel@esrf.fr and victor.puntes@icn.cat

Contents

S1. Sample characterization

Transmission Electron Microscope and size distribution.

TEM images were acquired with a JEOL 1010 Electron Microscope operating at an accelerating voltage of 80 kV. Samples for TEM were prepared by drop casting on carbon coated copper TEM grids and left solvent evaporate at room temperature. Afterwards, more than 500 particles from different images were computer-analyzed and measured for size distribution analysis (Fig. S1).

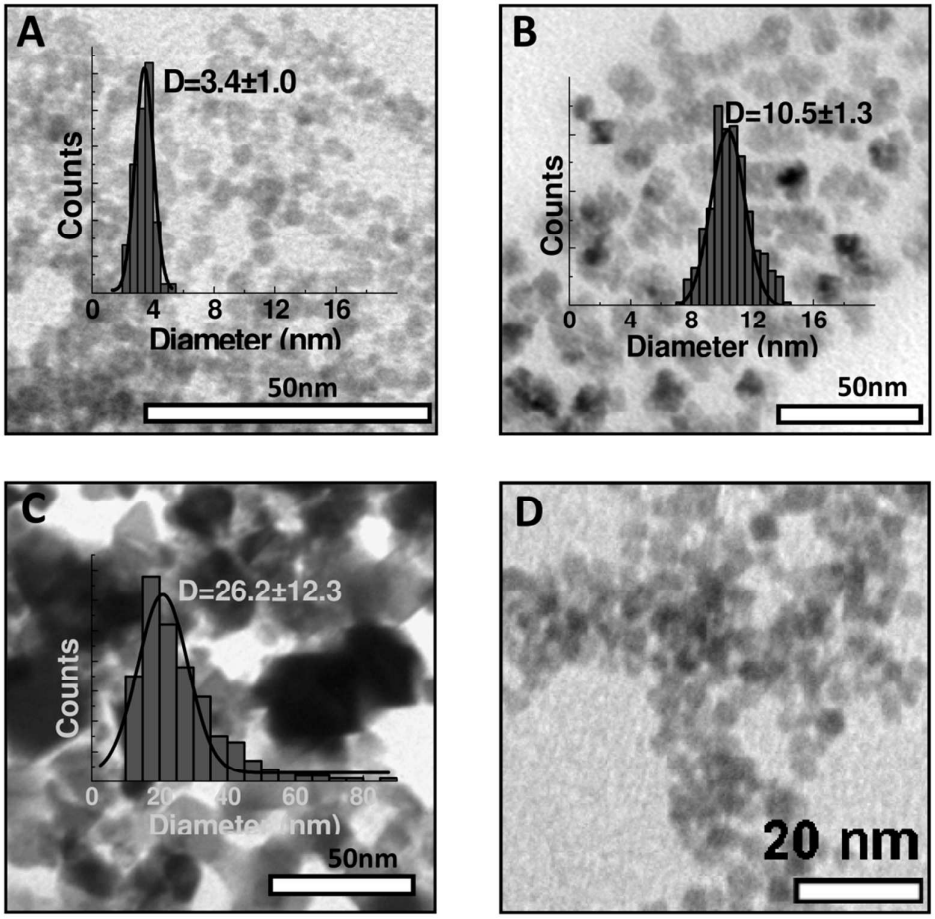

Figure S1. (A, B, C) TEM images and size distribution of the 3nm, 10nm and 25nm CeO_2 NPs respectively and (D) TEM image of the 3nm CeO_2 in H_2O_2.

X-Ray Diffraction.

X-Ray Diffraction (XRD) patterns were acquired with a PANalytical X'Pert diffractometer that uses a Cu Kα radiation source. Samples for XRD consist of the dry NPs in powder form.

For this purpose, destabilisation of the NPs mixing the colloidal NPs with a solvent of different polarity was followed by soft centrifugation after which NPs precipitated. The supernatant was discarded, and the pellet of NPs was dried to eliminate all the moisture (Fig. S2).

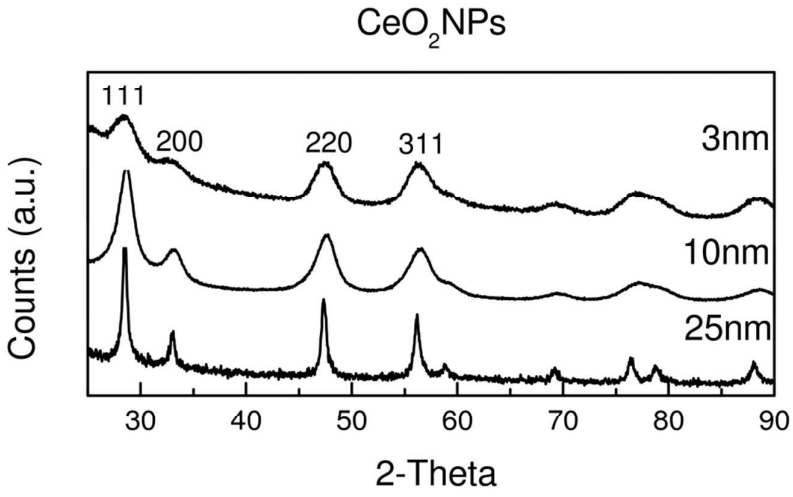

Figure S2. X-ray diffraction patterns of the 3nm, 10 nm and 25 nm CeO2 NPs respectively. The diffraction peaks corresponding to the (111), (200), (220) and (311) planes are characteristic for the cubic fluorite structure of CeO_2.[1]

Ultraviolet-visible spectroscopy.

UV-visible spectrophotometry (UV-Vis) spectra were acquired with a Shimadzu UV-2400 spectrophotometer. One ml of the NP solution was placed in a cuvette, and spectral analysis was performed in the 600 nm to 260 nm range (Fig. S3).

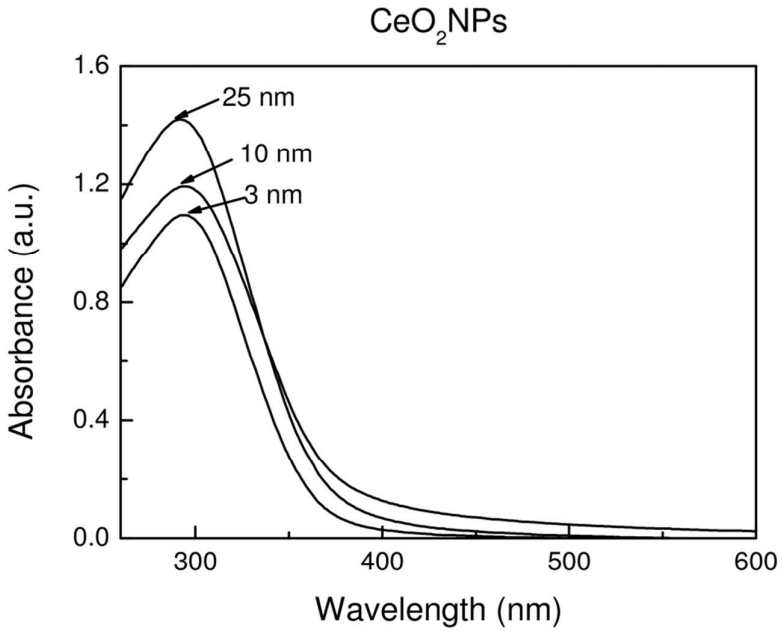

Figure S3. UV-Visible spectra of 3nm, 10nm and 25nm CeO_2 NPs. The spectra of all compounds present one strong absorption band [2].

S2. EXAFS analysis

The EXAFS spectra were analyzed using the IFEFFIT program package[3]. The pre-edge region was fitted by a linear function between -220 eV and -90 eV below the edge position and subtracted from the raw data. The EXAFS data were normalized to an edge jump of 1 using the range of 30–400 eV above the edge position. Fourier transforms to *R* space with a k^3 weighting factor and a Hanning window function were performed. The theoretical calculation of the scattering amplitudes and phase shift functions were done by using the FEFF8 program.[4] The first shell is due to single scattering paths corresponding to Ce-O (first shell, 2.3433 Å). The fit of the first (Ce-O) coordination shell was performed in *R* space for *k* weight = 3, *k* range = 2– 9.8 $Å^{-1}$, *dk* =1 and *R* = 1–2.5 Å, *dr* = 0.5. The energy shift was fixed to 3.46 eV for all fittings. The k^3-weighted EXAFS in k-space in the range 0-10 $Å^{-1}$ and k^3-weighted Fourier Transform (FT) magnitude spectra of the catalase mimetic activities of 3nm

CeO_2 and best fit (solid green lines) over the first Ce–O coordination shell are shown respectively in Figure S4. The results of the fit are given in Table S1.

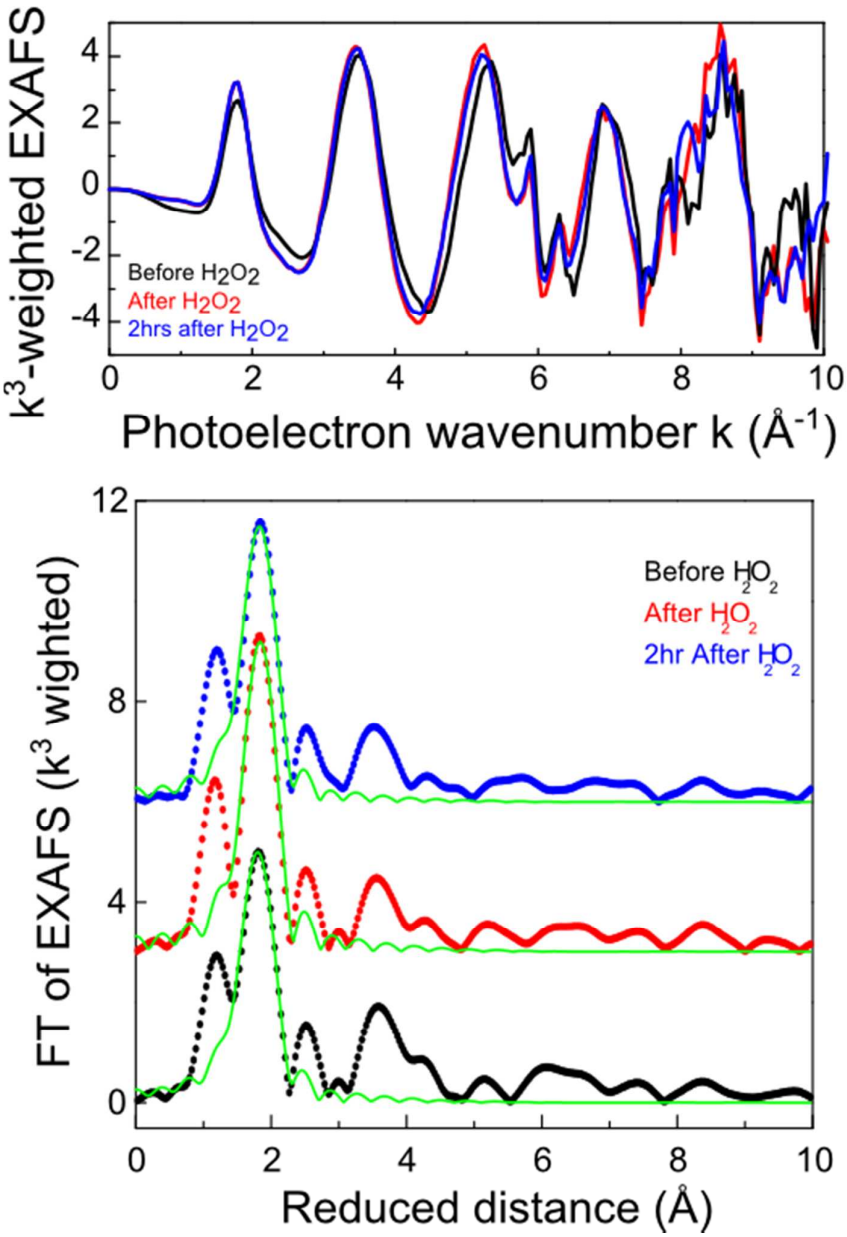

Figure S4. (A) k^3-Weighted EXAFS in the k-space and (B) k^3-Weighted Fourier Transform (FT) magnitude spectra and best fitting (solid green lines) over the first Ce–O coordination shell. A vertical offset (3 and 6) was applied for clarity.

Table S1: Coordination numbers (N), bond distance Ce-O first shell (R), the Debye-Waller Factor (σ^2) and relative error in the fit (R-factor) obtained from the EXAFS fits of 3nm CeO_2 NPs before, immediately after and 2hrs after the addition of H_2O_2 (the values in the bracket are errors).

3nm CeO_2	N	R(Å)	σ^2 (10^{-3} Å^2)	R-factor
Before H_2O_2	8	2.282 (0.008)	0.010 (0.003)	0.015
After H_2O_2	8	2.315 (0.007)	0.008 (0.002)	0.099
2hr after H_2O_2	8	2.310 (0.008)	0.009 (0.003)	0.013

S3. Radiation damage study

All colloidal solutions were characterised using a liquid jet set-up as shown in Figure 1. The jet diameter was 1 mm and exposed to air without any confinement. The volume of solution was about 60 ml. The beam size was of 150*600 μm^2 (vertical * horizontal). The jet speed was 4-5ml/s. The total time of data collection was 60 s per scan. No photo-reduction effect was observed when comparing consecutive scans. The total incident photon flux on the sample was 7 x10^{12} photons/second at 5.725 keV. The X-ray dose received by the sample per scan was 1x10^4 photons per μm^2 (assuming that all X-rays are absorbed) which is well below the limit established *e.g.* for X-ray sensitive proteins[5]. The exposure time of the CeO_2 NPs solution to the X-ray beam can be easily minimized using a liquid jet thus avoiding modification of the NPs due to radiation damage.

The experiments were repeated several times also in different environments:

a) colloidal solution using a free liquid jet as described above.
b) colloidal solution in a container under stirring where the incident beam passes through a window (Kapton™) and directly hits the solution (NP size effect and NP synthesis).
c) low temperature measurements (T=15 K) in a cryostat with He exchange gas (NP size effect).

The different sample environments gave identical results. However, significant modification of the Ce electronic structure with time was observed under the X-ray beam (radiation damage) for b) and c). We conclude that for the liquid jet, the available oxygen in the air does not alter the chemical state of the NPs. Measurements using the liquid jet set-up is favourable as it allows room temperature *in situ/operando* studies.

S4. Iterative Transformation Factor Analysis

Qualitative analysis to identify the Ce species involved in the *in situ* synthesis was performed by applying Iterative Transformation Factor Analysis (ITFA) to the normalized XANES spectra[6, 7]. This method combines principal component analysis (PCA), VARIMAX rotation and iterative target test (ITT). The qualitative analysis is done in three steps. In the first and second steps, a PCA procedure is used to determine and identify respectively the principal components if XANES spectra of pure reference components are available. In the third step, VARIMAX rotation and ITT procedures are used to determine the relative concentrations of the principal components in each sample spectrum and to derive real spectra of endmember species.

First step: The principal component analysis yields a set of eigenvectors ("abstract" spectra) and factor loadings ("abstract" concentrations), which represents the data in the n-dimensional factor space with an orthogonal basis defined by the eigenvectors. "Abstract" denotes that the eigenvectors and the factor loadings are not interpretable in terms of real spectra. In the first step of ITFA, the principal component analysis, the number of spectrally different components is determined without the need of any structural model. For this purpose, we used the theoretical root mean square error functions RE (real error), IE (imbedded)[8], and the semi-empirical indicator function IND developed by Malinowski[9]. All the functions depend on the number of components (n) employed for the abstract data reproduction. When the number of possible components is raised to its maximum value which is equal to the number of available spectra, the influence of the additional components on the data reproduction will diminish. For example, the IND function reaches a minimum at the number of principal components. While the first few components usually represent spectral differences, the following components represent only experimental error and can be neglected. The error functions, summarized in Table S2, can be used to determine the cut off between structural information and experimental error. For the samples (number 1-9 in Supplementary Tab. S2), the error in the data is RE(2) ~ 0.108 and the error in the reproduced data is IE(2) ~ 0.00589 (Supplementary Tab. S2). The data quality is improved by a factor RE(2)/IE(2) = 1.8 due to

the removal of the experimental noise represented by components 3 to 9. In the studied set of XANES spectra, the IND reaches a minimum for two components (Supplementary Fig. S5a). This is the evidence that only two components are present.

Second step: As a second step of ITFA, the chemical origin of the two components can be investigated by adding the spectra of possible reference compounds to the set of sorption spectra. When the spectrum of the $Ce(NO_3)_3.6H_2O$ was added, the IND function (Supplementary Fig. S5a) and the reproduction of all 9 spectra point to the presence of only two structural components. This indicates that $Ce(NO_3)_3.6H_2O$ is one component.

The second component could not be identified directly by this method due to a lack of appropriate reference spectra. However, because both the initial (Ce^{3+} ions) and the final (Ce^{4+} ions) phases should be present in the set of data as individual species, there is no room for the other phase, the second principal component is necessarily pure CeO_2 NPs essentially made of Ce^{4+} ions.

Third step: The third step of ITFA is the determination of the relative concentrations of the two components using the VARIMAX procedure and the iterative target test (ITT)[10, 11]. The VARIMAX procedure maximizes the sum of the squared factor loadings such that the basis of the factor space is rotated in a way that each factor has a small number of large loadings and a large number of zero or small loadings. This new representation of the data in the rotated factor space can be physically interpreted. By employing VARIMAX the rotated factor loadings correlate with the relative concentrations of the components in the spectra. The spectra with the highest or lowest amount of a component can be identified. The ITT uses this information finally for the calculation of relative concentrations.

In our case, the VARIMAX rotation for the first two components indicates that the first and the second component reach their maximum concentration at t=0h and t=23h respectively, the spectrum of pure CeO_2 phase can be calculated by ITT as 1-sum (of relative concentrations of the component 1 and to derive the spectra of the end-member species.)

So in the concentration test vector file, we assume the following information to generate the concentration test vectors by the ITT procedure:

Component 1: Spectrum 1, 100%

Component 2: will be calculated with 1-sum (of rel. concentrations of component 1).

Supplementary Figure S5b shows the abstract spectra of the two principal components obtained from the ITT procedure compared to the XANES spectra of $Ce(NO_3)_3.6H_2O$ and CeO_2 NPs. The abstract spectrum of pure CeO_2 and the experimental XANES spectrum of CeO_2 NPs are very similar, confirming that the CeO_2 NPs are essentially composed of Ce^{4+}

ions. The slight spectral difference is due to the removal of the experimental noise in the abstract spectrum. The XANES spectra of the *in situ* reaction, their best fit and residual using the calculated two-component target transforms and the weight fractions of each component extracted from these fits are shown in Supplementary Figures S5c,d respectively. Linear combinations of the abstract spectra of the two components reproduce closely all spectral features of each spectrum of the synthesis. This highlights the reliability of the approach.

Table S2: Principal component analysis of the *in situ* synthesis XANES spectra in the energy range 5715-5760 eV where n, RE(n), IE(n) and IND are respectively the number of components, the real error, the imbedded error and indicator function.

n	RE(n)	IE(n)	IND(n)
1	0.027	0.0119	0.00042
2	**0.011**	**0.0059**	**0.00022**
3	0.010	0.0064	0.00028
4	0.009	0.0066	0.00038
5	0.008	0.0067	0.00054
6	0.007	0.0073	0.00084
7	0.005	0.0081	0.00136
8	0.004	0.0083	0.00167

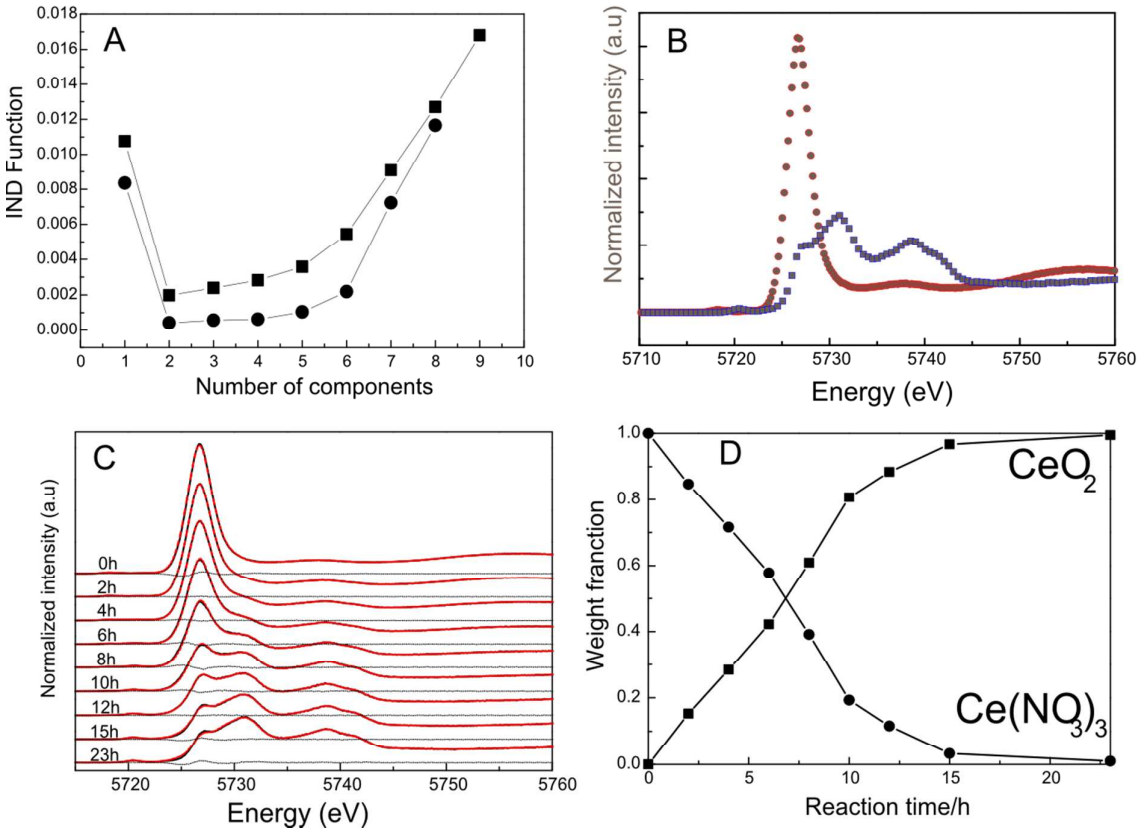

Figure S5. (A) Plot of the indicator (IND) function with the number of components (●). The XAS spectrum of $Ce(NO_3)_3.6H_2O$ was included in the set of XAS data as one of the reference spectrum and the IND function still minimizes for 2 components demonstrating that $Ce(NO_3)_3.6H_2O$ is one of the reference compound (■). (B) XAS spectra of $Ce(NO_3)_3.6H_2O$ and CeO_2 NPs of the *in situ* synthesis (red and blue dots respectively) compared to calculated two-component target transformed spectra using the two principal components extracted from the XAS data set (black line). (C) Reproduction (red line) of the experimental data (black line) using the isolated spectra of components 1 and 2 and residual (black line) obtained from ITFA. (D) Weight fraction of Ce^{3+} and Ce^{4+} ions during the *in situ* synthesis of CeO_2 NPs obtained from ITFA.

S5. Estimation of the effective number of f-electrons, n_f.

The program FITYK was applied for peak fitting using the Levenberg–Marquard algorithm for nonlinear least square optimization[12, 13]. For all the XANES spectra, the fitting procedure was as follow[14-17]:

a) The edge jump (corresponding to excitations into the continuum) was fitted and normalized to unity with an arctangent function. This fit was done separately from the fitting of the resonant excitations into the Ce 5d states.
b) The fitting energy range was selected and fixed to 5726-5743 eV.
c) Two split Gaussian functions were used to fit the $2p^5 4f^0 5d^1$ (peaks C and D; in the following abbreviated f^0) and $2p^5 4f^1 \underline{L} 5d^1$ (peaks A and B; in the following abbreviated $f^1\underline{L}$) absorption resonances, respectively.

Different model functions (symmetric Gaussians or Lorentzians) were also tested but the best fitting with the minimum error and minimum model functions was achieved when using split Gaussian functions. In the case of curve fitting using symmetric Gaussian and/or Lorentzian model functions, more than 6 functions are needed to reproduce the XANES spectrum and the larger number of parameters introduces higher ambiguity in the fitting (*vide infra*).

Once the first XANES spectrum has been fitted, the parameters obtained are stored in the program to fit the other XANES spectrum of the series. This leads to small relative errors within one series. The absolute error for the areas is less important (*vide infra*). Figure S6a shows the XANES spectrum of the 3nm CeO_2 NPs fitted using four split Gaussian peaks together with an arctangent function.

The assignment of the features in the Ce L_3 XANES is based on the single impurity Anderson model (SIAM)[18].This model is also used to analyze data using 3d X-ray photoelectron spectroscopy (XPS) that is frequently employed to determine the amount of Ce^{3+} in nanoceria[19]. The fundamental assumption in this model is that the ground state bonding state $\left|\Psi_b^g\right\rangle$ of Ce in CeO_2 must be described by a linear combination of electron configurations:

$$\left|\Psi_b^g\right\rangle = \cos\beta\left|f^0\right\rangle - \sin\beta\left|f^1\underline{L}\right\rangle \qquad \text{(Equation 1)}$$

This approach assumes charge transfer from a ligand orbital to Ce *f* leaving a hole on the ligand ($\underline{L}$). The orbital mixing explains the strong charge transfer excitations in X-ray spectra of ceria[20]. It has been questioned whether the atomic-like Ce 4f orbitals are actually populated or whether the valence band has extended covalent states with f symmetry[21]. Many authors insist that the Ce 4f levels are empty in the ground state.[22, 23] This unresolved controversy is irrelevant in the present context because our analysis of the L_3 main edge concerns the electron density over the entire ceria NP.

The *f*-electron occupancy for Ce is estimated by taking the weighted area (A) of the absorption resonances and is given by the equation[14-17, 20]:

$$n_{4f} = \frac{ACe(f^1\underline{L})}{ACe(f^1\underline{L}) + ACe(f^0)} \qquad \text{(Equation 2)}$$

The number of f electrons n_f is not a "good" quantum number and thus no quantum mechanical observable. The absolute values obtained for n_f depend on the model to describe the electronic structure and Equation 2 therefore has to be seen in the context of SIAM. The interpretation in the present study uses the relative change of n_f over the course of the chemical reaction that we can determine with sufficient accuracy. Table S3 presents the weighted areas of the f^0 and $f^1\underline{L}$ absorption resonances and n_f estimated using Equation 1 for the 3nm CeO_2 NPs during the catalase mimetic activity.

We obtained an estimate of the absolute error for the areas and n_f by varying the fitting models (4 split Gaussians, 4 and 6 symmetric Gaussians, 4 and 6 Lorentzians). The areas varied by ±0.8 and n_f by ±0.07. The relative variation of n_f within one series of spectra keeping the fitting model and starting parameters fixed is negligible, *i.e.* the development of n_f when H_2O_2 is added as shown in Figure 3a is not influenced by the large absolute error.

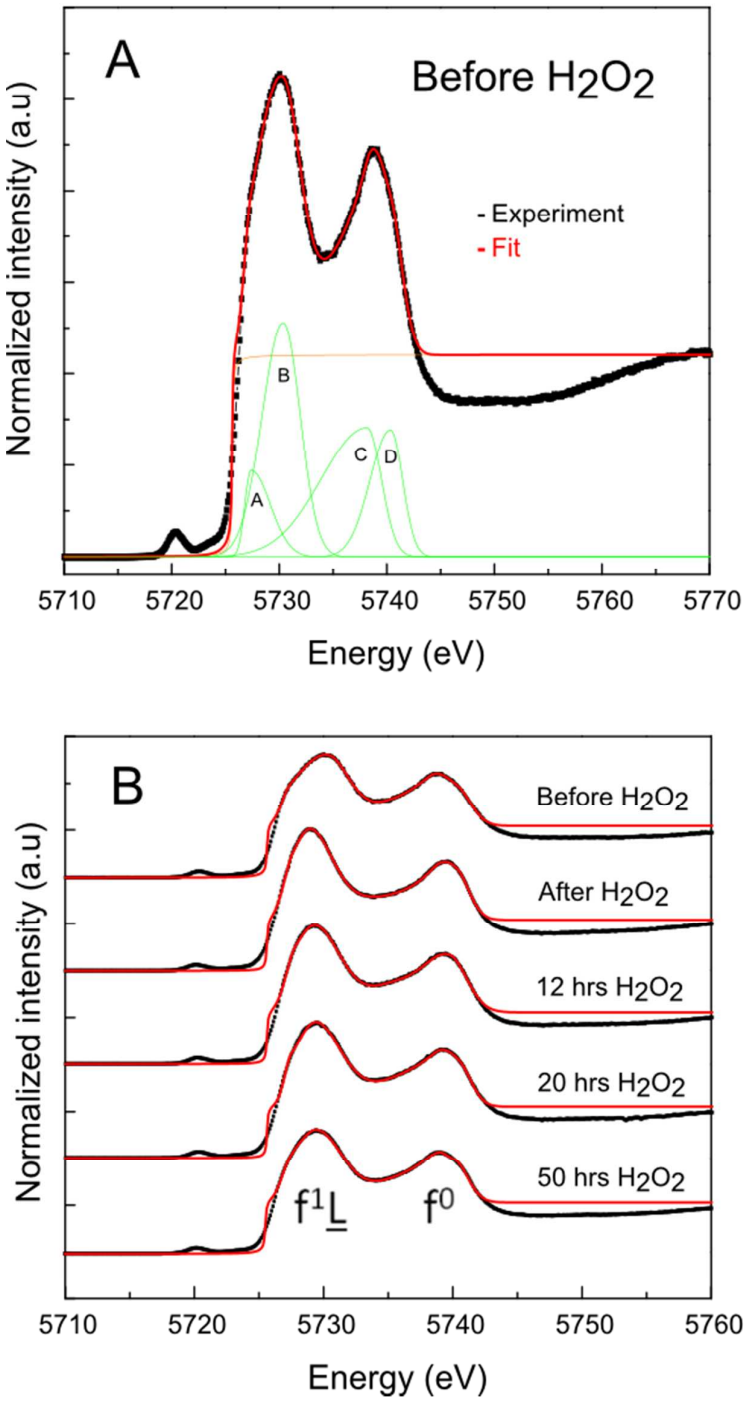

Figure S6. (A) Experimental (black) and theoretical fit (red curve) of Ce L_3 edge XANES spectrum of 3nm CeO_2 before addition of H_2O_2 using split Gaussian peaks to model the two absorption resonances, together with an arctangent function as a representative example. (B) Experimental (black) and theoretical fit (red curve) of Ce L_3 edge XANES spectra of 3nm CeO_2 before and after the addition of H_2O_2, 12hrs, 20hrs and 50hrs after the addition of H_2O_2.

3nm CeO_2	$A(f^0)$	$A(f^1\underline{L})$	n_f
Before H_2O_2	7.54	7.07	0.48
After H_2O_2	6.65	8.85	0.57
12hrs Later	7.27	8.84	0.55
20hrs Later	7.27	8.22	0.53
50hrs Later	7.17	7.07	0.50

Table S3: Weighted areas of the f^0 and $f^1\underline{L}$ absorption resonances and the number of f electrons n_f estimated using Equation 2 for the 3nm CeO_2 NPs during the catalase mimetic activity. The absolute and relative errors are discussed in the text.

S6. Synthesis of the 3nm CeO_2 colloidal NPs

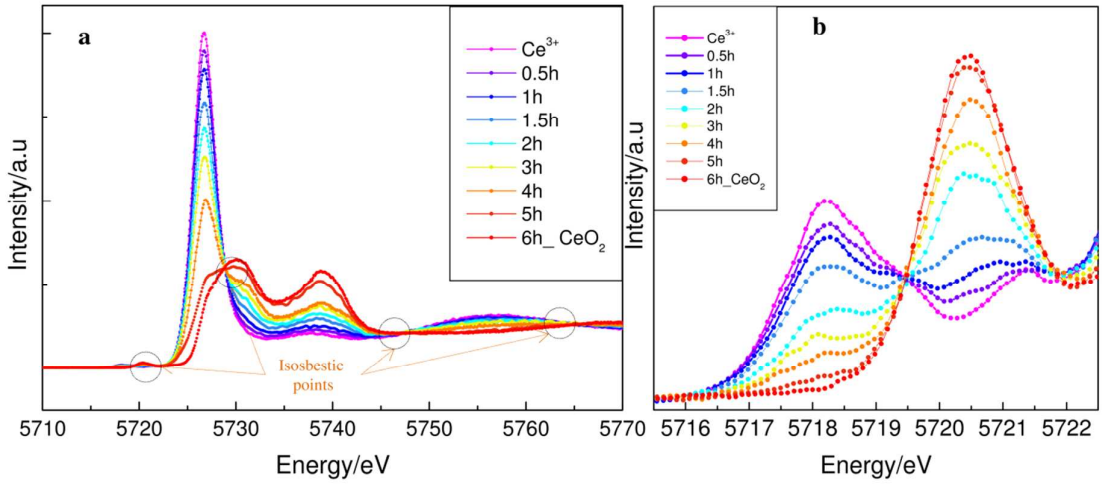

Figure S7. (a) Time dependent high-energy-resolution Ce L_3 XAS spectra recorded during the *in situ* synthesis of 3 nm CeO_2 NPs. (b) Enlargement of the pre-edge region.

S7. Evolution of the pH of the 3nm, 10nm and 25nm CeO_2 NPs

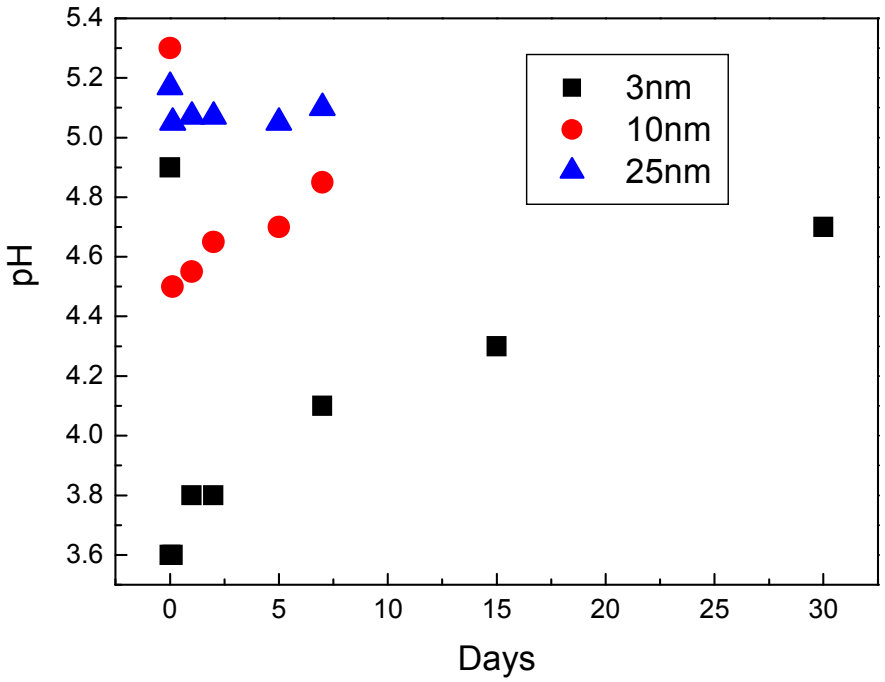

Figure S8. Time dependence of the pH during the catalase mimetic activity of the 3nm, 10nm and 25 CeO_2 NPs. The pH evolution of the 10nm and 25nm CeO_2 NPs were studied for a period of 1 week.

References

1. Hu, C. G.; Zhang, Z. W.; Liu, H.; Gao, P. X.; Wang, Z. L. Direct Synthesis and Structure Characterization of Ultrafine CeO_2 Nanoparticles. *Nanotechnology* **2006,** *17*, 5983-5987.

2. Ho, C. M.; Yu, J. C.; Kwong, T.; Mak, A. C.; Lai, S. Y. Morphology-Controllable Synthesis of Mesoporous CeO_2 Nano- and Microstructures. *Chem. Mater.* **2005,** *17*, 4514-4522.

3. Ravel, B.; Newville, M. Athena, Artemis, Hephaestus: Data Analysis for X-Ray Absorption Spectroscopy Using Ifeffit. *J. Synchrotron Rad.* **2005,** *12*, 537-541.

4. Ankudinov, A. L.; Nesvizhskii, A. I.; Rehr, J. J. Dynamic Screening Effects in X-Ray Absorption Spectra. *Phys. Rev. B* **2003,** *67*, 115120.

5. Yano, J.; Kern, J.; Irrgang, K. D.; Latimer, M. J.; Bergmann, U.; Glatzel, P.; Pushkar, Y.; Biesiadka, J.; Loll, B.; Sauer, K. *et al.* X-Ray Damage to the Mn_4ca Complex in Single Crystals of Photosystem II: A Case Study for Metalloprotein Crystallography. *P. Natl. Acad. Sci. USA* 2005, *102*, 12047-12052.

6. Rossberg, A.; Reich, T.; Bernhard, G. Complexation of Uranium(VI) with Protocatechuic Acid - Application of Iterative Transformation Factor Analysis to EXAFS Spectroscopy. *Anal. Bioanal. Chem.* 2003, *376*, 631-638.

7. Rossberg, A.; Ulrich, K. U.; Weiss, S.; Tsushima, S.; Hiemstra, T.; Scheinost, A. C. Identification of Uranyl Surface Complexes an Ferrihydrite: Advanced EXAFS Data Analysis and Cd-Music Modeling. *Environ. Sci. Technol.* 2009, *43*, 1400-1406

8. Malinowski, E. R. Theory of Error in Factor-Analysis. *Anal. Chem.* 1977, *49*, 606-612.

9. Malinowski, E. R. Determination of Number of Factors and Experimental Error in a Data Matrix. *Anal. Chem.* 1977, *49*, 612-617.

10. Brayden, T. H.; Poropatic, P. A.; Watanabe, J. L. Iterative Target Testing for Calculation of Missing Data Points. *Anal. Chem.* 1988, *60*, 1154-1158.

11. Kaiser, H. F. The Varimax Criterion for Analytic Rotation in Factor Analysis. *Psychometrika* 1958, *23*, 187-200.

12. Wojdyr, M. *See* http://www.unipress.waw.pl/fityk/.

13. Levy, N.; Burke, S. A.; Meaker, K. L.; Panlasigui, M.; Zettl, A.; Guinea, F.; Neto, A. H. C.; Crommie, M. F. Strain-Induced Pseudo-Magnetic Fields Greater Than 300 Tesla in Graphene Nanobubbles. *Science* 2010, *329*, 544-547.

14. Wu, Z. H.; Zhang, J.; Benfield, R. E.; Ding, Y. F.; Grandjean, D.; Zhang, Z. L.; Ju, X. Structure and Chemical Transformation in Cerium Oxide Nanoparticles Coated by Surfactant Cetyltrimethylammonium Bromide (Ctab): An X-Ray Absorption Spectroscopic Study. *J. Phys. Chem. B* 2002, *106*, 4569-4577.

15. Rueff, J. P.; Itié, J. P.; Taguchi, M.; Hague, C. F.; Mariot, J. M.; Delaunay, R.; Kappler, J. P.; Jaouen, N. Probing the Gamma-Alpha Transition in Bulk Ce under Pressure: A Direct Investigation by Resonant Inelastic X-Ray Scattering. *Phys. Rev. Lett.* **2006,** *96*, 237403.

16. Dallera, C.; Grioni, M.; Shukla, A.; Vanko, G.; Sarrao, J. L.; Rueff, J. P.; Cox, D. L. New Spectroscopy Solves an Old Puzzle: The Kondo Scale in Heavy Fermions. *Phys. Rev. Lett.* **2002,** *88*, 196403-196407.

17. Wu, Z. H.; Benfield, R. E.; Guo, L.; Li, H. J.; Yang, Q. L.; Grandjean, D.; Li, Q. S.; Zhu, H. S. Cerium Oxide Nanoparticles Coated by Surfactant Sodium Bis(2-Ethylhexyl) Sulphosuccinate (Aot): Local Atomic Structures and X-Ray Absorption Spectroscopic Studies. *J. Phys.Cond. Matter* **2001,** *13*, 5269-5283.

18. Gunnarsson, O.; Schonhammer, K. Electron Spectroscopies for Ce Compounds in the Impurity Model. *Phys. Rev. B* **1983,** *28*, 4315-4341.

19. Fujimori, A. Mixed-Valent Ground-State of CeO_2. *Phys. Rev. B* **1983,** *28*, 2281-2283.

20. Bianconi, A.; Marcelli, A.; Dexpert, H.; Karnatak, R.; Kotani, A.; Jo, T.; Petiau, J. Specific Intermediate-Valence State of Insulating 4f Compounds Detected by L_3 X-Ray Absorption. *Phys. Rev. B* **1987,** *35*, 806-812.

21. Wuilloud, E.; Delley, B.; Schneider, W. D.; Baer, Y. Spectroscopic Evidence for Localized and Extended F-Symmetry States in CeO_2. *Phys. Rev. Lett.* **1984,** *53*, 202-205.

22. Goubin, F.; Rocquefelte, X.; Whangbo, M. H.; Montardi, Y.; Brec, R.; Jobic, S. Experimental and Theoretical Characterization of the Optical Properties of CeO_2, $SrCeO_3$, and Sr_2CeO_4 Containing Ce^{4+} (F(0)) Ions. *Chem. Mater.* **2004,** *16*, 662-669.

23. Sham, T. K.; Gordon, R. A.; Heald, S. M. Resonant Inelastic X-Ray Scattering at the Ce L_3 Edge of $CePO_4$ and CeO_2: Implications for the Valence of CeO_2 and Related Phenomena. *Phys. Rev. B* **2005,** *72*, 35113-35119.